The effect of gas-phase transport on Marangoni convection in volatile binary fluids

Tongran Qin and Roman O. Grigoriev
School of Physics, Georgia Institute of Technology, Atlanta, GA 30332-0430, USA

Recent experimental and numerical studies of convection in confined layers of volatile binary liquids with a free surface subjected to a horizontal temperature gradient have observed a reversal in the direction of interfacial flow as the concentration of air in the vapor space above the liquid is decreased. These observations suggests that transport in the gas phase has a significant effect on the balance between thermocapillary and solutocapillary stresses, the competition of between which determines the flow direction. In order to develop a quantitative description of the flow reversal, we use the two-sided (liquid/gas) transport model introduced previously to obtain approximate analytical solutions for the interfacial temperature and composition of the liquid, which control the thermocapillary and solutocapillary stresses. Despite the complex nature of this problem, our theoretical predictions agree well with the results of numerical simulations, which indicates that our analysis captures the essential physics of the problem.

I. INTRODUCTION

It is well-known that surface tension effects play a dominant role in microscale fluid flows in terrestrial conditions and even at macroscopic scales in microgravity. In particular, thermocapillary stresses which arise at the free surface of nonisothermal fluids case the flow in the direction opposite to the thermal gradient. In some practical applications, such as in thermal management devices that rely on phase change, thermocapillarity plays an adverse role, leading to dry-out of the hot regions meant to be cooled by the evaporating liquid. The direction of the flow can be reversed by using volatile binary liquids, such as water-alcohol mixtures, where the more volatile component has a lower surface tension [1]. The flow reversal in such binary liquids is due to the solutocapillary effect, which is caused by interfacial concentration gradients and can oppose thermocapillarity.

While thermocapillary stresses arise for any fluids, simple or binary, volatile or nonvolatile, solutocapillary stresses of comparable magnitude can only arise in volatile binary liquids. The strength of solutocapillary stresses depends on both the mean composition of the liquid and the composition of surrounding gas or, more specifically, the presence of noncondensables, such as air. The latter are well-known to suppress phase change, which plays a crucial role in generating a concentration gradient at the free surface. Recent experimental [2] and numerical [3] studies have investigated the dependence of the flow in a layer of methanol-water mixture on the composition of the two phases characterized by the mean concentration of methanol $\bar{Y}_m$ in the liquid and the mean concentration of air $\bar{X}_a$ in the gas. It was determined that the flow is most sensitive to the composition of the gas phase: flow reversal requires $\bar{X}_a$ to be very low (a few percent or less). The dependence on the composition of the liquid phase was found to be much weaker, with the solutocapillary effect being somewhat stronger at low values of $\bar{Y}_m$.

The resolution of those two studies, however, was too low to determine the optimal values of $\bar{X}_a$ and $\bar{Y}_m$ which would generate the strongest flow in the direction of the applied temperature gradient. More importantly, our fundamental understanding of the interplay between phase change at the liquid-vapor interface and the transport of heat and mass and the flow in the two layers remains limited. While there is abundant literature on Marangoni-driven flows in nonvolatile fluids (the readers are referred to Ref. [3] which presents a detailed overview) none of it is directly relevant here.

The objective of this paper is to obtain approximate analytical solutions of the comprehensive two-sided transport model introduced in Ref. [3], which will quantify the Marangoni stresses driving the flow and their dependence on the composition of the liquid and gas phase. The outline of the present study is as follows. We describe the system being investigated in Section II. The analysis of the transport model is presented in Section III, with the analytical predictions compared with the numerical results. The summary and conclusions are presented in Section IV.

II. PROBLEM STATEMENT

We will consider a flow in a layer of volatile binary liquid (water-methanol mixture) with a free surface confined along with its vapor and air in a rectangular test cell (cf. Fig. 1). The flow is driven by a horizontal temperature gradient in the extended (x) direction created by imposing a temperature difference $\Delta T = T_h - T_c$ between the outer surfaces of the two end walls. Previous studies of this problem [2, 3] showed that the liquid-vapor interface has a low curvature and the flow is nearly two-dimensional, so we will simplify the problem by considering the liquid layer to have a uniform thickness and the flow to be strictly two-dimensional.

The flow in both phases is assumed incompressible

$$\nabla \cdot \mathbf{u} = 0, \tag{1}$$

and the momentum transport in the bulk is described by the Navier-Stokes equation with the Boussinesq approx-

FIG. 1. The test cell containing the liquid and air/vapor mixture. Gravity is pointing in the negative z direction. The shape of the contact line reflects the curvature of the free surface for a liquid wetting the walls. The inner dimensions are $H = W = 10$ mm, $L = 48.5$ mm, the walls are 1.25 mm thick, and the liquid (gas) layer has a thickness $d_l = 2.5$ mm ($d_g = 7.5$ mm).

imation

$$\rho\left(\partial_t \mathbf{u} + \mathbf{u}\cdot\nabla\mathbf{u}\right) = -\nabla p + \mu\nabla^2\mathbf{u} + \rho\mathbf{g}, \tag{2}$$

where $\mathbf{u}$ is the velocity, p is the pressure, ρ and μ are the density and dynamic viscosity of the fluid, respectively, and $\mathbf{g} = -g\hat{z}$ is the gravitational acceleration. Heat transport in the bulk is described by the advection-diffusion equation

$$\partial_t T + \mathbf{u}\cdot\nabla T = \alpha\nabla^2 T, \tag{3}$$

where T is the temperature and $\alpha = k/\rho C_p$ is the thermal diffusivity of the fluid. Mass transport in the binary liquid mixture is described by the advection-diffusion equation for the concentration Y_b ($b = m$ for methanol and $b = w$ for water)

$$\partial_t Y_b + \mathbf{u}\cdot\nabla Y_b = \nabla\cdot(D_l\nabla Y_b), \tag{4}$$

where D_l is the binary mass diffusivity. In the ternary gas phase, mass transport is described using a similar equation

$$\partial_t X_b + \mathbf{u}\cdot\nabla X_b = \nabla\cdot(\mathfrak{D}_b\nabla X_b), \tag{5}$$

where X_b is the concentration of component b in the gas phase and $\mathfrak{D}_b$ is the effective mass diffusivity [4].

The evolution equations (1)-(5) are solved subject to the appropriate boundary conditions at the liquid-gas interface and the inner surfaces of the cavity walls. At the interface, standard boundary conditions account for the balance of momentum, heat, and mass fluxes across the interface. In particular, the stress balance

$$(\mathbf{\Sigma}_l - \mathbf{\Sigma}_g)\cdot\hat{\mathbf{n}} = \hat{\mathbf{x}}\partial_x\sigma, \tag{6}$$

where

$$\mathbf{\Sigma} = \mu\left[\nabla\mathbf{u} + (\nabla\mathbf{u})^T\right] - p\mathbb{I} \tag{7}$$

is the stress tensor, couples the fluid flow to the temperature and concentration fields due to the dependence of the surface tension σ on their interfacial profiles, resulting in Marangoni (thermo- and solutocapillary) stresses.

Local phase equilibrium is described with Raoult's law

$$p_{g,b} = p_g X_b = \gamma_b p_{s,b} Y_b, \tag{8}$$

where γ_b is the activity coefficient of component b, which accounts for deviations from an ideal liquid mixture, $p_{g,b}$ and p_g are the partial and total pressure in the gas phase. The saturation vapor pressure $p_{s,b}$ of a pure component b can be related to the interfacial temperature T_i via the Antoine equation

$$\ln p_{s,b} = A_b - \frac{B_b}{C_b + T_i}, \tag{9}$$

where A_b, B_b, and C_b are empirical coefficients. By defining the latent heat $\mathcal{L}_b$

$$\mathcal{L}_b = T_b R_b, \tag{10}$$

where $R_b = R/M_b$ is the specific gas constant, M_b is the molar mass, and temperature scales

$$T_b = \frac{B_b T_0^2}{(C_b + T_0)^2}, \tag{11}$$

the Antoine equation can be rewritten in the form of the more popular Clausius-Clapeyron relation

$$\ln\frac{p_{s,b}}{p^0_{s,b}} = -T_b\left(\frac{1}{T_s} - \frac{1}{T_0}\right), \tag{12}$$

where $p^0_{s,b}$ is the reference value of the saturation vapor pressure for pure component b at the reference temperature T_0. Finally, the number density flux describing phase change at the interface is given by [3]

$$j_{b,i} = \frac{2\chi_b}{2-\chi_b} n_g X_b u_t \frac{T_b}{T_i}\frac{T_i - T_{s,b}}{T_{s,b}}, \tag{13}$$

where n_g is the number density of the gas, $\chi_b = O(1)$ is the accommodation coefficient, and

$$u_t = \sqrt{\frac{R_b T_i}{2\pi}} \tag{14}$$

it the characteristic thermal velocity. Additional details of the mathematical model and its numerical implementation are discussed in Ref. [3].

Before delving into the analysis of the model, which has been found to give a fairly accurate description of the experiment, let us sketch the plan of attack. A quick look at the transport equations for the momentum, heat, and mass shows that the flow, temperature, and concentration fields are all coupled via advection, buoyancy, or various boundary conditions, and hence have to be solved for simultaneously, making this problem extremely complicated. Our previous investigation of a similar problem involving a volatile simple liquid confined in a moderate aspect-ratio cavity [5] came to an interesting and

unexpected conclusion, however. Numerical simulations showed that, despite this coupling, mass transport in the gas phase appears to be effectively one-dimensional and independent of the flow field even for relatively high mass Péclet numbers. This result allows dramatic simplification, since the concentration profile in the gas phase determines the interfacial temperature via (9) and hence the thermocapillary stresses. This allows one to find the flow in the liquid layer, then the flow in the gas layer and, finally, the temperature field in both phases.

As our numerical simulations [3] and the analysis presented in the next section confirm, for a volatile binary liquid, mass transport in the gas phase is also essentially one-dimensional. Hence, once the concentration fields X_m and X_w in the gas phase are found, we can determine both the interfacial temperature T_i and the interfacial composition Y_m via (8) and (9). These interfacial profiles determine the thermo- and solutocapillary stresses and hence the flow in the liquid layer. In particular, the direction of the flow along the interface can be determined by comparing the strength of the thermocapillary stresses and the (opposing) solutocapillary stresses. (While buoyancy is nonnegligible for a few-mm-thick layer of liquid considered in Refs. [2, 3], it mainly affects the stability of the flow [6].) Once the flow in the liquid layer is found, the remaining undetermined fields can be computed from the corresponding transport equations similarly to the simple liquid problem.

III. RESULTS

The previous numerical simulations [3] were performed for the temperature differential $\Delta T = 6$ K used in the experiments of Li and Yoda [2]. At this relatively high ΔT, in both studies the flow was found to be unsteady for intermediate values of the mean air concentration $\bar{X}_a$. The present study uses numerical simulations at a lower $\Delta T = 2$ K and $\bar{Y}_m = 0.6$ (i.e., 60% methanol 40% water) for which the flow is steady over the entire range of $\bar{X}_a$ as a reference to compare with the model predictions.

A. Mass transport in the gas phase

Our previous investigation [5] has shown that mass transport in the binary (vapor/air) gas mixture in local equilibrium with a layer of volatile simple liquid confined inside a moderate aspect-ratio cavity is well-described by the one-dimensional theory of filmwise condensation on a vertical cold surface [7] even when there is significant flow in the gas phase and when condensation takes place near, but not actually on, the cold wall. A similar result also holds for the case of binary liquids investigated here, where the gas is a ternary mixture.

Let us introduce the rescaled coordinates $\chi = x/d_g$ and $\zeta = z/d_g$, such that the gas phase corresponds to $0 < \zeta < 1$ and $0 < x < \Gamma_g$, where $\Gamma_g = L/d_g$ is the aspect ratio of the gas layer. Since the flow field is constrained to the $\chi - \zeta$ plane and is incompressible, it can be written in terms of the stream function $\psi(\chi, \zeta)$,

$$\mathbf{u}_g = \hat{\mathbf{x}}\partial_\zeta\psi - \hat{\mathbf{z}}\partial_\chi\psi. \tag{15}$$

Assuming phase change in the central region of the cavity is negligible and the aspect ratio Γ_g is relatively large (in this study $\Gamma_g \approx 6.5$), the gas flow can be considered essentially horizontal there

$$\mathbf{u}_g = u_x\hat{\mathbf{x}} + u_z\hat{\mathbf{z}} \approx u_x\hat{\mathbf{x}}, \tag{16}$$

where $u_z/u_x = O(\Gamma_g^{-1})$. Numerical simulations (cf. Fig. 2) illustrate that this is an accurate assumption over the entire range of $\bar{X}_a$. Therefore, the mass transport equation (5) in steady state reduces to

$$d_g u_x \partial_\chi X_b = \mathfrak{D}_b(\partial_\chi^2 X_b + \partial_\zeta^2 X_b), \tag{17}$$

where the vertical component u_z of the velocity yields a higher order correction and can be neglected. On the other hand, the horizontal component

$$u_x = \bar{u} + \tilde{u}_x(\chi, \zeta) \tag{18}$$

could be decomposed into the mean flow $\bar{u}$ and zero-mean recirculation flow $\tilde{u}_x$,

$$\int_0^1 \tilde{u}_x d\zeta = 0. \tag{19}$$

Respectively, the stream function can decomposed as

$$\psi = \bar{u}\zeta + \tilde{\psi}, \tag{20}$$

where $\partial_\zeta\tilde{\psi} = \tilde{u}_x$, such that

$$\int_0^1 \partial_\zeta\tilde{\psi} d\zeta = \tilde{\psi}|_{\zeta=1} - \tilde{\psi}|_{\zeta=0} = 0. \tag{21}$$

Since phase change at the liquid-gas interface is assumed negligible in the central region of the cavity, no-flux boundary condition $\partial_\zeta X_b = 0$ for the concentration of both vapors can be used at the interface $\zeta = 0$ and the top wall $\zeta = 1$. Setting $u_x = \bar{u}$ (i.e., $\tilde{u}_x = 0$) and solving (17) subject to these boundary conditions reproduces the solution previously obtained in Ref. [5]

$$X_b = C_0 + C_1 e^{-Pe_m\chi}, \tag{22}$$

where

$$Pe_m = \frac{|\bar{u}|d_g}{\mathfrak{D}_b} \tag{23}$$

is the mass Péclet number corresponding to the mean flow and the constants $C_0 > 0$ and $C_1 < 0$ can be determined by the boundary conditions at $\chi = 0$ and $\chi = \Gamma_g$. In the general case (i.e., $\tilde{u}_x \neq 0$) the solution to (17) is

$$X_b = C_0 + C_1 e^{-Pe_m\chi}[1 + g(\zeta)], \tag{24}$$

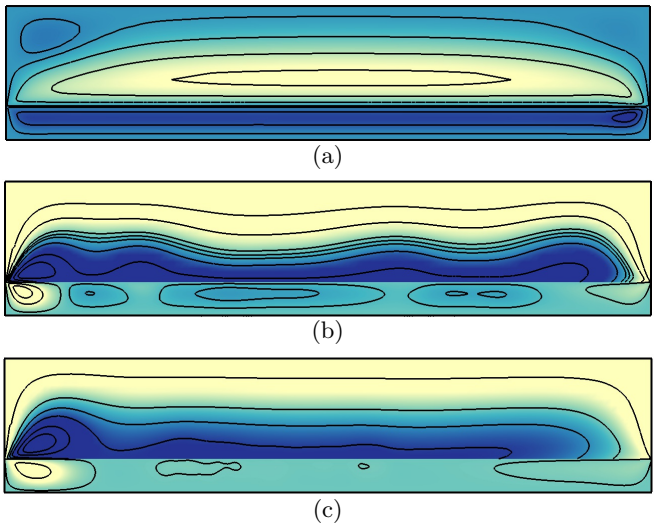

FIG. 2. Fluid flow in both phases at $\Delta T = 2$ K, $\bar{Y}_m = 0.6$ with (a) $\bar{X}_a = 0.7$, (b) $\bar{X}_a = 0.1$, (c) $\bar{X}_a = 0.015$. The cold end wall is on the left. Solid lines represent the streamlines of the flow; color corresponds to the values of ψ.

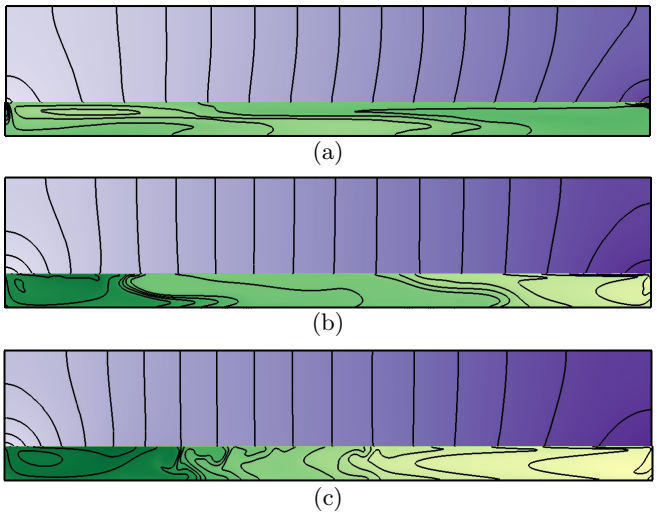

FIG. 3. Concentration of methanol in the liquid and in the gas at $\Delta T = 2$ K and $\bar{Y}_m = 0.6$ for different $\bar{X}_a$. (a) $\bar{X}_a = 0.7$, $Y_m = 0.6 \pm 2.88 \times 10^{-4}$, $X_m = 0.26 \pm 0.023$, (b) $\bar{X}_a = 0.1$, $Y_m = 0.6 \pm 9.31 \times 10^{-4}$, $X_m = 0.43 \pm 0.037$, (c) $\bar{X}_a = 0.015$, $Y_m = 0.6 \pm 6.95 \times 10^{-3}$, $X_m = 0.78 \pm 0.039$. Solid lines represent equispaced level sets of the concentration fields (15 in the liquid and 20 in the gas). In both phases, the lighter (darker) color indicates lower (higher) concentration.

where

$$g''(\zeta) = \frac{\bar{u}\tilde{u}_x(\zeta)d_g^2}{\mathfrak{D}_b^2}[1 + g(\zeta)]. \tag{25}$$

The right-hand-side of (25), and hence $g(\zeta)$ itself, is of order $\epsilon = Pe_m Pe_r$, where

$$Pe_r = \max_\zeta \frac{|\tilde{u}_x| d_g}{\mathfrak{D}_b} \tag{26}$$

is the Péclet number describing the strength of the recirculation flow $\tilde{u}$. Specifically,

$$g(\zeta) = \frac{\bar{u}d_g^2}{\mathfrak{D}_b^2}\int \tilde{\psi}(\zeta)d\zeta + O(\epsilon^2). \tag{27}$$

Now, finally, the reason for separating u_x into the two components $\bar{u}$ and $\tilde{u}_x$ becomes clear: the no-flux boundary condition for X_b requires $g'(0) = g'(1) = 0$ which is only consistent with (27) when (21) is satisfied. Here the recirculation flow $\tilde{u}$ can be thought of as a perturbation of the mean flow $\bar{u}$, an interpretation which will become useful in the next Section.

The crucial observation is that ϵ remains small regardless of the mean concentration $\bar{X}_a$ of air: Pe_r becomes small in the limit $\bar{X}_a \to 0$ (due to an increase in the effective mass diffusivities with decreasing pressure), while Pe_m becomes small in the limit $\bar{X}_a \to 1$ (due to the decrease in $\bar{u}$). For small ϵ, the z-dependence of the concentration field is weak, hence the solution (22) remains a good approximation even when Pe_r is not small. Indeed, this is consistent with the results of numerical simulations. As Fig. 3 shows, in the central region of the cavity, the variation of the concentration in the vertical direction is negligible compared with that in the horizontal direction.

We can compare the analytical and numerical results quantitatively. The mean flow velocity in the gas can be written as

$$\bar{u} = -\frac{\bar{j}_m + \bar{j}_w}{n_g}, \tag{28}$$

where $\bar{j}_b$ is the mean (depth-averaged) value of the number flux of the vapor of component b. Since phase change occurs over the entire liquid-vapor interface, the mean flux

$$\bar{j}_b(x) = \frac{1}{d_g}\int_x^L j_{b,i}(x')\,dx' \tag{29}$$

is a function of the horizontal position. However, evaporation (condensation) takes place mainly near the hot (cold) wall, so that function becomes essentially constant $\bar{j}_b(x) \approx \bar{j}_b^c$ in the central region of the cavity (cf. Fig. 4), where

$$\bar{j}_b^c = \max_x \bar{j}_b(x). \tag{30}$$

We will therefore use the values given by (30) in (28) and drop the superscript c in the subsequent discussion where this does not cause confusion.

Let us consider the dependence of the mean fluxes $\bar{j}_b$ on the concentration of air next. The description of mass transport based on effective diffusivity allows us to decouple the equations for the concentrations of the three

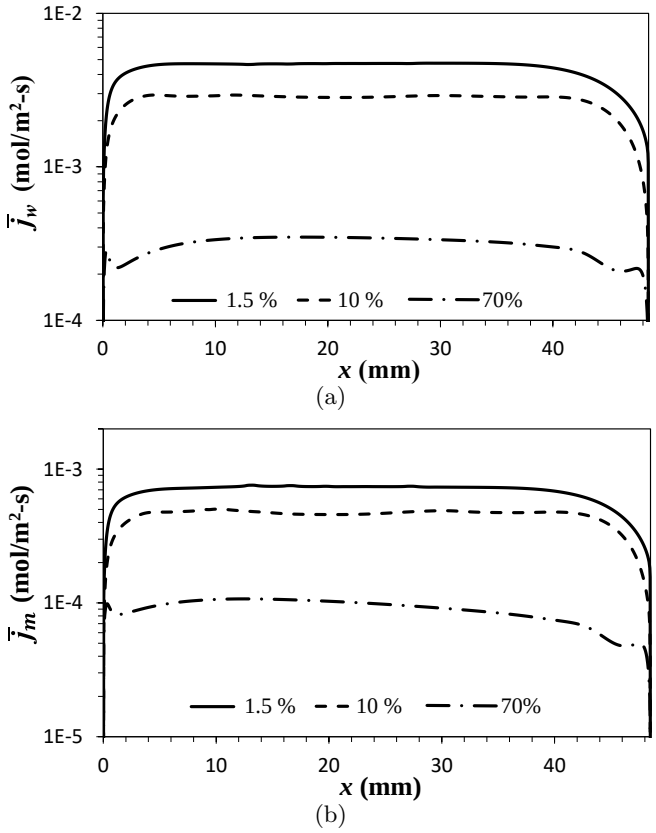

FIG. 4. Mean number flux $\bar{j}_b$ (29) across the vertical cross-section of the cavity for (a) methanol and (b) water, at $\Delta T = 2$ K and $\bar{Y}_m = 0.6$ with different mean concentrations of air $\bar{X}_a$: $\bar{X}_a = 0.015$ (solid line), $\bar{X}_a = 0.1$ (dashed line) and $\bar{X}_a = 0.7$ (dotted line).

components (water and methonol vapor and air). The resulting equations are formally identical to the transport equation for a single vapor in a binary mixture with air. Therefore, we can treat the heat and mass transport associated with each vapor component independently. Assuming that the layer of liquid at the bottom of the cavity has a negligible contribution to the overall heat transport dominated by the latent heat associated with phase change, we can use a generalization of the corresponding result for the binary gas mixture to write the condensation flux for component b

$$\bar{j}_b = \frac{\Delta T}{\mathcal{L}_b M_b Z_b}, \tag{31}$$

in terms of the net thermal resistance

$$Z_b = Z_o + Z_{d,b}, \tag{32}$$

where Z_o is the thermal resistance due to conduction in the liquid and the walls and the interfacial resistance, and $Z_{d,b}$ is the diffusive resistance of the gas layer. While Z_o can be considered independent of the air concentration, $Z_{d,b}$ is an increasing function of $\bar{X}_a$.

To compute the diffusive resistance, we note that, since mass transport is essentially one-dimensional in the central portion of the cavity, in steady state the horizontal components of the flux of each component vapor satisfy

$$\begin{aligned} \bar{j}_m &= n_g \mathfrak{D}_m \partial_x X_m - n_g \bar{u} X_m, \\ \bar{j}_w &= n_g \mathfrak{D}_w \partial_x X_w - n_g \bar{u} X_w. \end{aligned} \tag{33}$$

Solving this system of equations together with (28) yields

$$\begin{aligned} \bar{j}_m &= \frac{n_g}{X_a}\left[\mathfrak{D}_m(1-X_w)\partial_x X_m + \mathfrak{D}_w X_m \partial_x X_w\right], \\ \bar{j}_w &= \frac{n_g}{X_a}\left[\mathfrak{D}_w(1-X_m)\partial_x X_w + \mathfrak{D}_m X_w \partial_x X_m\right]. \end{aligned} \tag{34}$$

The concentration gradient $\partial_x X_b$ can be related to the gradient of partial pressure $p_{g,b}$ and the saturation pressure of the pure component $p_{s,b}$ through Raoult's law (8)

$$\partial_x X_b = \frac{1}{p_g}\partial_x p_{g,b} = \frac{\gamma_b \bar{Y}_b}{p_g}\partial_x p_{s,b}, \tag{35}$$

where we assume the total pressure p_g to be constant and the variation of liquid concentration about the mean value $\bar{Y}_b$ to be negligible. The saturation pressure gradient $\partial_x p_{s,b}$ can be found from the Antoine equation (12) yielding

$$\partial_x X_b = X_b \frac{T_b}{T_0^2}\tau, \tag{36}$$

where τ is the interfacial temperature gradient. Substitution of the mean values for all the concentrations yields

$$\begin{aligned} \bar{j}_m &= \frac{n_g \tau}{\bar{X}_a T_0^2}\left[\mathfrak{D}_m(1-\bar{X}_w)\bar{X}_m T_m + \mathfrak{D}_w \bar{X}_m \bar{X}_w T_w\right], \\ \bar{j}_w &= \frac{n_g \tau}{\bar{X}_a T_0^2}\left[\mathfrak{D}_w(1-\bar{X}_m)\bar{X}_w T_w + \mathfrak{D}_m \bar{X}_w \bar{X}_m T_m\right]. \end{aligned} \tag{37}$$

The walls of the test cell are good thermal conductors compared with both the liquid and the gas. Hence, in the limit $\Delta T \to 0$ and $\bar{X}_a \to 1$, the temperature gradient $\tau \to \Delta T/L$ and $Z_{d,b} \gg Z_o$, such that (31) and (37) yield

$$\begin{aligned} Z_{d,m} &= \frac{\bar{X}_a T_0^3 L}{p_g T_m}\left[\mathfrak{D}_m(1-\bar{X}_w)\bar{X}_m T_m + \mathfrak{D}_w \bar{X}_m \bar{X}_w T_w\right]^{-1}, \\ Z_{d,w} &= \frac{\bar{X}_a T_0^3 L}{p_g T_w}\left[\mathfrak{D}_w(1-\bar{X}_m)\bar{X}_w T_w + \mathfrak{D}_m \bar{X}_w \bar{X}_m T_m\right]^{-1}. \end{aligned} \tag{38}$$

Note that, in the limit $\bar{X}_w \to 0$ ($\bar{X}_m \to 0$), the diffusive resistance $Z_{d,m}$ ($Z_{d,w}$) reduces to the expression $Z_d = L/k_c$, where k_c is the effective condensation thermal conductivity derived for a binary (vapor/air) mixture by Peterson *et al.* [8].

Finally, Z_o can be found from (31), since in the limit $\bar{X}_a \to 0$ we have $Z_{d,b} \to 0$, which allows our analytical predictions to be compared directly with the corresponding numerical results [3]. Fig. 5 shows that the analytical

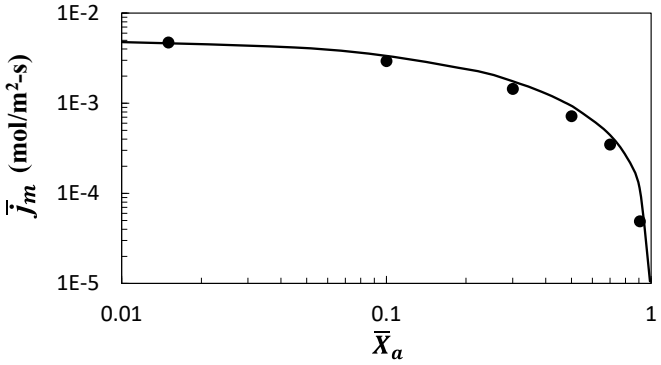

FIG. 5. Characteristic molar flux $\bar{j}_m$ for methanol as a function of $\bar{X}_a$ at $\Delta T = 2$ K and $\bar{Y}_m = 0.6$. Solid line represents the analytical estimate based on (31), symbols – numerical results obtained using (30).

and numerical results are in reasonable agreement, suggesting that the one-dimensional description of transport in the gas phase is reasonably accurate. An increase in $\bar{X}_a$ leads to an increase in the diffusive resistance for both component vapors and, correspondingly, a decrease in both fluxes. The minor discrepancy between the numerical and analytical results is likely due to the contribution of advection in the liquid layer that has been ignored in our analysis.

Once the mean vapor fluxes and the mean flow velocity have been determined from (28) and (31), we can finally compare the analytical prediction (22) for the concentration profiles with the numerical results. As Fig. 6 shows, we find good agreement (minor deviations will be discussed in the next Section). In general, the concentrations of all components in the ternary gas mixture vary exponentially with x, which is consistent with the findings for simple fluids with binary (vapor/air) gas mixtures [5]. The exponential concentration profiles become approximately linear when $Pe_m \ll \Gamma_g^{-1}$. This limit corresponds to low values of the mean flow velocity $\bar{u}$ and hence low values of ΔT and/or high values of $\bar{X}_a$. In particular, at $\Delta T = 2$ K, the concentration profiles are nearly linear for all $\bar{X}_a$.

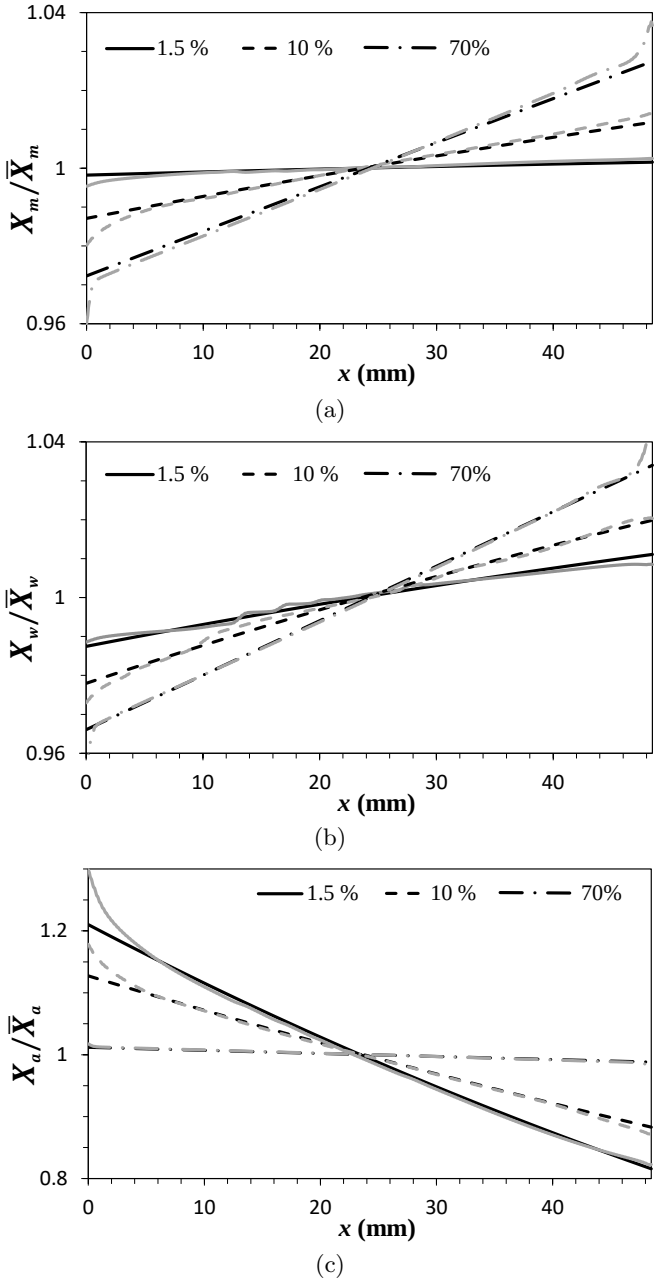

FIG. 6. Normalized concentration profiles in the gas phase at $\Delta T = 2$ K for methanol (a), water (b), and air (c) with $\bar{Y}_m = 0.6$ and different $\bar{X}_a$. Numerical and analytical results are represented by gray and black lines, respectively. Numerical results correspond to the middle of the gas layer.

B. Interfacial temperature and concentration profiles

The concentration fields in the gas phase determine the temperature and liquid concentration at the interface. First of all, note that equation (13) implies that the interfacial temperature is essentially equal to the saturation temperature, $T_i \approx T_{s,m} \approx T_{s,w}$, due to the large values of the ratio T_b/T_i (for water and methanol, $T_w = 4.9 \times 10^3$ K and $T_m = 2.8 \times 10^3$ K) and low values of u_g/u_t [9]. Raoult's law (8), which is the statement of local phase equilibrium, requires

$$\frac{p_{s,b}}{p_{s,b}^0} = \frac{X_b}{Y_b}\frac{Y_b^0}{X_b^0}, \tag{39}$$

where the superscript 0 denotes the reference values corresponding to the global thermodynamic equilibrium at $T = T_0$. Choosing T_0 as the mean temperature, we can replace the reference values of all the concentrations with

the mean values, $Y_b^0 = \bar{Y}_b$ and $X_b^0 = \bar{X}_b$. One the other hand, Antoine equation (12) requires

$$\frac{p_{s,b}}{p_{s,b}^0} = e^{T_b/\theta}, \tag{40}$$

where we have defined a new variable θ according to

$$\frac{1}{\theta} = \frac{1}{T_0} - \frac{1}{T_i}. \tag{41}$$

Equating the right-hand-sides of (39) and (40), we find

$$Y_b = \frac{X_b \bar{Y}_b}{\bar{X}_b} e^{-T_b/\theta}. \tag{42}$$

Since the liquid is a binary mixture,

$$\frac{X_m \bar{Y}_m}{\bar{X}_m} e^{-T_m/\theta} + \frac{X_w \bar{Y}_w}{\bar{X}_w} e^{-T_w/\theta} = 1. \tag{43}$$

This transcendental equation for θ can be solved approximately for small deviations of the interfacial temperature from T_0, i.e., for $|\theta| \gg \min(T_m, T_w)$ by Taylor-expanding both exponential terms.

In this study, $|\theta| \geq O(T_0^2/\Delta T) = O(10^4 \text{ K})$ for ΔT as large as 10 K. The actual temperature variation along the interface is typically a fraction of ΔT, leading to an even higher $|\theta|$ (e.g., $|\theta| \sim O(10^5 \text{ K})$ at $\Delta T = 2$ K), so that reasonably accurate results can be obtained in analytic form by truncating the Taylor series at linear terms, which yields

$$\frac{1}{\theta} = -\frac{a_0}{a_1}, \tag{44}$$

where

$$a_0 = 1 - \frac{X_m \bar{Y}_m}{\bar{X}_m} - \frac{X_w \bar{Y}_w}{\bar{X}_w},$$
$$a_1 = T_m \frac{X_m \bar{Y}_m}{\bar{X}_m} + T_w \frac{X_w \bar{Y}_w}{\bar{X}_w}. \tag{45}$$

The corresponding interfacial temperature can now be found from (41) and the interfacial concentrations of water and methanol in the liquid phase from (42).

The analytical predictions for the interfacial temperature are in reasonable agreement with the numerical results (cf. Fig. 7). As (36) suggests, the temperature gradient is related to the gas concentration gradient, so the nearly linear concentration profiles at $\Delta T = 2$ K implies nearly linear interfacial temperature profiles for all $\bar{X}_a$. The predicted interfacial concentration profiles, however, deviate noticeably from those found in the numerical simulations, as Fig. 8 illustrates. The is due to the insufficient accuracy in our description of the concentration fields in the gas phase. Even though the analytical and numerical results appear to agree quite well (cf. Fig. 6), even relatively small discrepancies are greatly amplified because of the exponential dependence of Y_b on the ratio

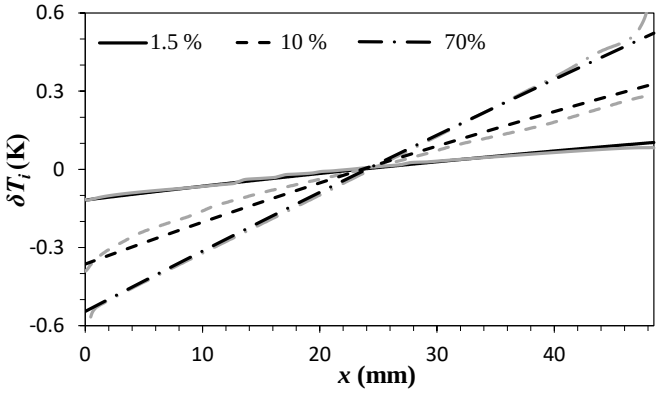

FIG. 7. Interfacial temperature for different $\bar{X}_a$ at $\bar{Y}_m = 0.6$ and $\Delta T = 2$ K. The variation $\delta T_i = T_i - T_0$ about the mean is plotted. Numerical and analytical results are represented by gray and black lines, respectively.

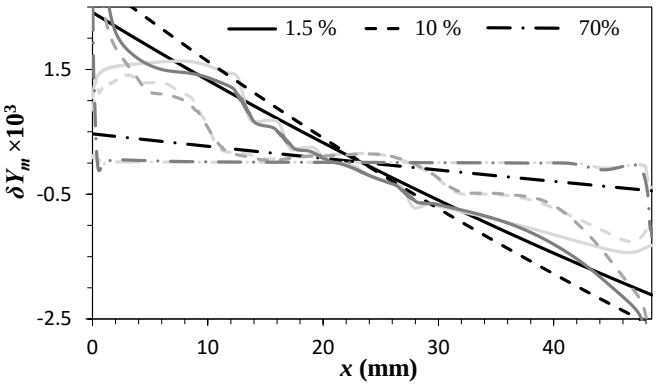

FIG. 8. The interfacial concentration of methanol in the liquid for different $\bar{X}_a$ at $\bar{Y}_m = 0.6$ and $\Delta T = 2$ K. The vertical axis shows the variation $\delta Y_m = Y_m - \bar{Y}_m$ about the mean. Black lines represent the analytical estimate (42) based on the analytical solution for X_m and T_i, dark gray lines – the numerical results, and light gray lines – the analytical estimate (42) based on the numerical results for X_m and T_i.

T_b/θ in (42). To illustrate this, we computed the interfacial profile of the methanol concentration in the liquid by substituting numerical, rather than analytical, results for the concentration fields X_m and X_w into equation (42). As Fig. 8 shows, the resulting estimate accurately reproduces even the fine details of the numerical solution for Y_m in the central region of the cavity, confirming that it is indeed the accuracy of the estimate (22) that is the culprit. (The remaining discrepancy near the end walls is mainly due to the difference between T_i and $T_{s,b}$.)

The origin of the small deviation of the analytical solution (22) from the numerical one can be easily identified by inspecting the flow field, methanol concentration in the liquid, and the phase change flux at the interface. The particular flow shown in Fig. 9 features several convection rolls in the liquid layer. The composition of the liquid layer is controlled by advection, which dominates over diffusion due to a very low value of D_l (and a corre-

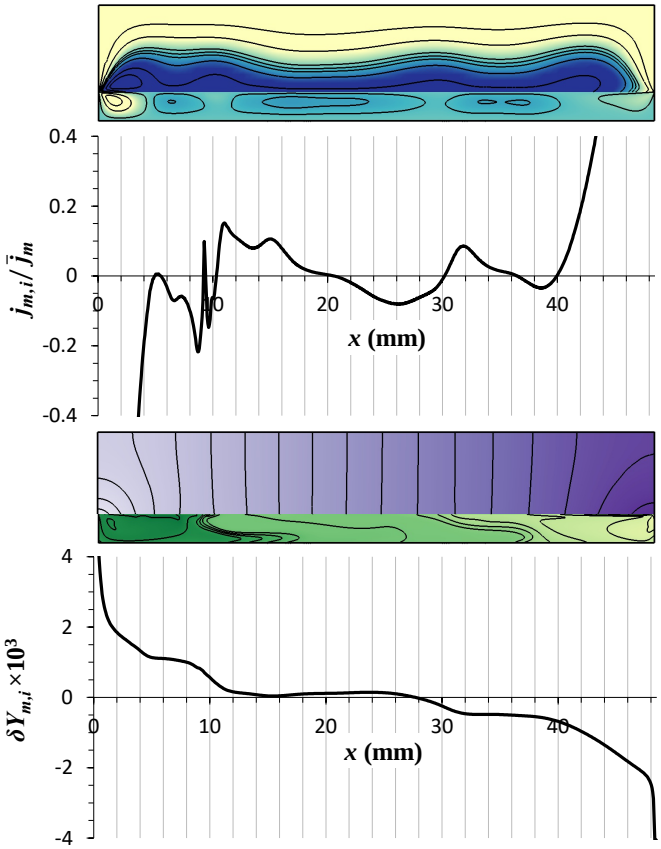

FIG. 9. Numerical solutions for $\bar{X}_a = 0.1$, $\bar{Y}_m = 0.6$ and $\Delta T = 2$ K. The panels shows (from top to bottom) the flow field, the normalized molar mass flux associated with the condensation/evaporation of methanol, the concentration of methanol in both phgases, and the variation δY_m of the methanol concentration in the liquid about the mean.

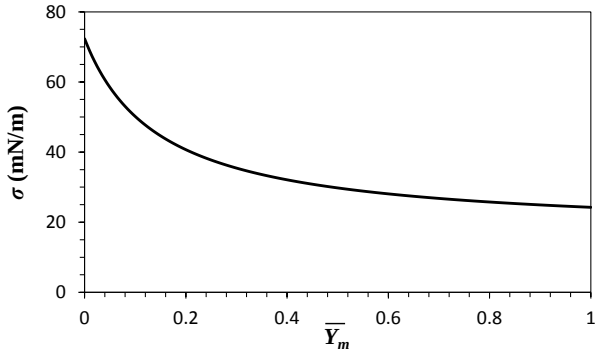

FIG. 10. Surface tension σ for the methanol-water mixture as a function of the methanol concentration $\bar{Y}_m$ computed using (46).

spondingly large mass Péclet number). Convection rolls effectively convert the horizontal gradient of Y_m driving the mean flow into the vertical gradient.

The analysis presented in Section III A completely ignored phase change in the central region of the cavity. However, even though it is far less intense than near the end walls, phase change also occurs in that central region. The vertical mass flux in the liquid layer causes evaporation at the left edge of each counter-rotating convection roll and condensation at the right edge, as demonstrated by the phase change flux $j_{m,i}$. This phase change acts as a perturbation on the flow field in the gas layer (the clearly visible modulation of the stream lines in the top panel of Fig. 9). As the relation (27) illustrates, a perturbation in the flow field generates a corresponding perturbation in the concentration fields X_b described by (25) and it is this perturbation that is responsible for the deviation of the predicted composition of the liquid at the interface from the actual composition that is observed (bottom panel of Fig. 9).

The spatial variation in the temperature and composition of the liquid at the interface generates thermocapillary and solutocapillary stresses, respectively. These stresses will be discussed in more detail next, but we conclude this Section by noting that our analysis points to the perturbation in Y_m, shown in the bottom panel of Fig. 9, causing both the phase change in the central region of the cavity and the modulation of solutocapillary stresses that give rise to the convection rolls. The detailed stability analysis of this problem that couples the perturbations in the flow and composition of both layers is outside the scope of this paper, although the mechanism of the instability appears to be clear.

C. The Marangoni stresses and the flow

With the solutions for the interfacial temperature and concentration profiles in hand, we can immediately determine the thermocapillary and solutocapillary stresses. The surface tension of the methanol-water liquid mixture is not a simple linear combination of the surface tensions of the two pure substances. Instead, it is predicted using an empirical expression [10] based on the fits to experimental data

$$\sigma = f(Y_m)\sigma_m + [1 - f(Y_m)]\sigma_w, \tag{46}$$

where

$$f(Y_m) = Y_m \frac{1 + c_1(1 - Y_m)}{1 - c_2(1 - Y_m)}, \tag{47}$$

with empirical parameters c_1 and c_2. The result is shown in Fig. 10. The surface tension of each component is assumed to be a linear function of temperature

$$\sigma_b = \sigma_b^0 - \sigma_b'(T_i - T_0), \tag{48}$$

where σ_b^0 is the surface tension of the pure substance at the reference temperature T_0 and $\sigma_b' = -\partial\sigma_b/\partial T_i$ is the temperature coefficient of surface tension for component b.

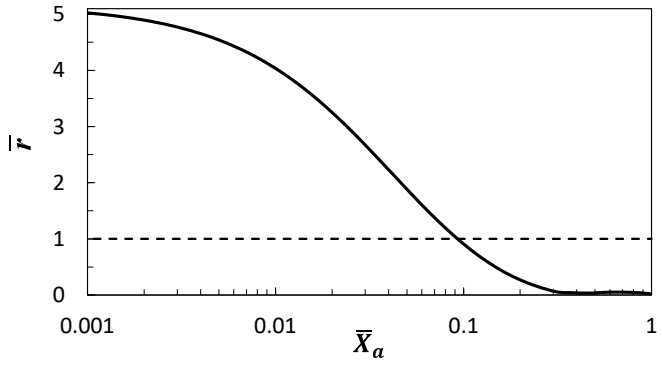

FIG. 11. The ratio of solutocapillary and thermocapillary stresses for different $\bar{X}_a$ at $\bar{Y}_m = 0.6$ and $\Delta T = 2$ K evaluated using (54) with mean values of $\partial_x X_m$ and $\partial_x T_i$. The dashed line represents the exact balance between the mean solutocapillary and thermocapillary stresses, $\bar{r} = 1$.

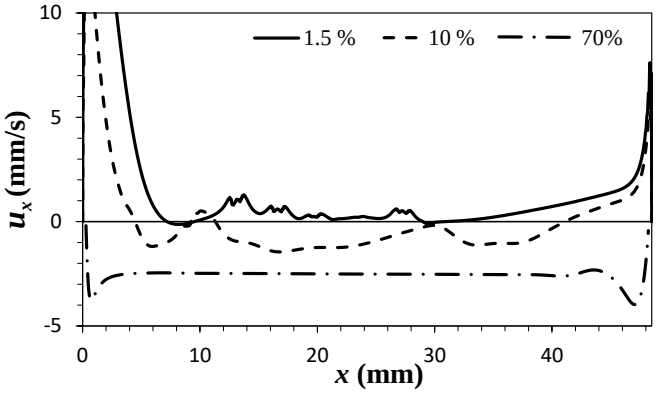

FIG. 12. Interfacial velocity at $\Delta T = 2$ K, $\bar{Y}_m = 0.6$ with different $\bar{X}_a$.

The net surface stress $\partial_x \sigma = \Sigma_S + \Sigma_T$ is the sum of the solutocapillary stress

$$\Sigma_S = F_S \partial_x Y_m \tag{49}$$

and thermocapillary stress

$$\Sigma_T = F_T \partial_x T_i, \tag{50}$$

where we have defined

$$F_S = f'(Y_m)(\sigma_m - \sigma_w) < 0, \tag{51}$$

and

$$F_T = -f(Y_m)\sigma'_m - (1 - f(Y_m))\sigma'_w < 0. \tag{52}$$

Taking the derivative of (42) we obtain

$$\partial_x Y_b \approx \frac{\bar{Y}_b}{\bar{X}_b}\left[\partial_x X_b - \frac{X_b T_b}{T_i^2}\partial_x T_i\right] e^{-\frac{T_b}{\theta}}, \tag{53}$$

which yields the following estimate for the ratio of solutocapillary and thermocapillary stresses

$$r \equiv -\frac{\Sigma_S}{\Sigma_T} \approx \frac{F_S}{F_T}\frac{\bar{Y}_m}{\bar{X}_m}\left[\frac{X_m T_m}{T_i^2} - \frac{\partial_x X_m}{\partial_x T_i}\right] e^{-\frac{T_m}{\theta}}, \tag{54}$$

where the minus sign reflects their (typically) opposite direction. When both concentration and temperature profiles are nearly linear, the derivatives $\partial_x X_m$ and $\partial_x T_i$ are nearly constant, so r does not vary significantly along the interface. At lower air concentrations, however, $\partial_x Y_m$ can vary considerably and can even change sign, as shown in Fig. 9. Hence it will be convenient to quantify the relative strength of the two stresses using the ratio of the mean values, $\bar{r}$, shown in Fig. 11, which corresponds to the mean values of $\partial_x X_m$ and $\partial_x T_i$ in (54).

In the limit $\bar{X}_a \to 1$ (e.g., at ambient conditions), the differential phase change responsible for generating solutocapillary stresses is greatly suppressed, such that $Y_m \to \bar{Y}_m$ and consequently $\Sigma_S \to 0$, which means that the flow is controlled entirely by thermocapillary stresses. The numerical results (cf. Fig. 12) show that the flow at the interface is indeed towards the cold end ($u_i < 0$) along the entire interface, with a nearly constant velocity in the central region of the cavity, which is consistent with a nearly constant temperature gradient.

As $\bar{X}_a$ decreases, the ratio $\bar{r}$ increases, reflecting the increase of solutocapillarity stresses associated with increased differential phase change. The mean solutoand thermocapillary stresses become comparable, $\bar{r} = 1$, around $\bar{X}_a = 0.1$, at which point we find the flow reversing its direction at multiple locations along the interface (cf. Fig. 12), depending on whether the local value of r is above or below unity. This is consistent with the pattern of convection rolls shown in Fig. 9. As the concentration of air is reduced even further, $\bar{r}$ increases above unity (e.g., $\bar{r} \approx 4$ at $\bar{X}_a = 0.015$), reflecting the dominant role of solutocapillary stresses. Correspondingly, the flow is found towards the hot wall along almost the entire interface.

The limit $\bar{X}_a \to 0$ is the most interesting from the perspective of evaporative cooling, where solutocapillarity can ameliorate the adverse effect of thermocapillary stresses leading to dry-out. In this limit $X_m + X_w = 1$, so that

$$\partial_x X_m = -\partial_x X_w, \tag{55}$$

and

$$e^{-T_b/\theta} \approx 1, \tag{56}$$

which allows us to make further progress. Combining the relation (53) for both water and methanol with (55) and (56), we find

$$r = \frac{F_S}{F_T}\frac{\bar{X}_m T_m + \bar{X}_w T_w}{T_0^2}\left(\frac{\bar{X}_m}{\bar{Y}_m} - \frac{\bar{X}_w}{\bar{Y}_w}\right)^{-1}. \tag{57}$$

This result predicts that the ratio of solutocapillary and thermocapillary stresses becomes constant in the limit

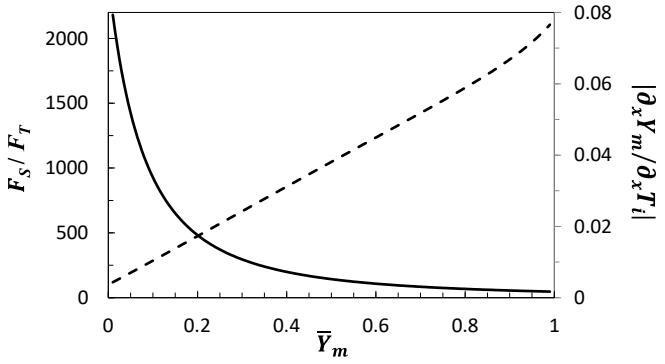

FIG. 13. The ratio of the coefficient F_S/F_T (solid line) and the gradients $\partial_x Y_m/\partial_x T_i$ (dashed line) at $\bar{X}_a = 0$.

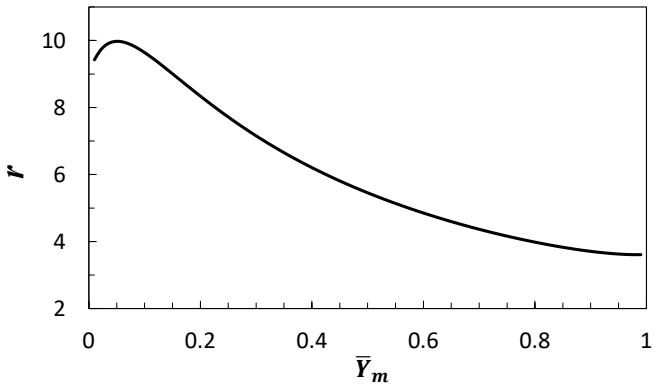

FIG. 14. The ratio of the solutocapillary and thermocapillary stresses for different $\bar{Y}_m$ at $\bar{X}_a = 0$.

$\bar{X}_a \to 0$, so the flow should become strictly unidirectional, just like in the opposite limit $\bar{X}_a \to 1$, but with the opposite direction.

As Fig. 13 illustrates, for water-methanol mixture, the ratio F_s/F_T is a monotonically decreasing function of $\bar{Y}_m$, while the ratio of the concentration and temperature gradients $|\partial_x \bar{Y}_m/\partial_x \bar{T}_i|$ is a monotonically increasing function, so predicting the trend for r is not straightforward. Evaluating the product of these two ratios shows that r has a peak value around 10 at $\bar{Y}_m \approx 0.05$ (cf. Fig. 14), which represents the optimal composition of the liquid which maximizes the favorable solutocapillary stresses.

As discussed in Section III B, although the analytical solution for the interfacial concentration profile that ignores phase change in the central region of the cavity does not give an accurate local prediction for solutocapillary stresses, the mean ratio $\bar{r}$ correctly predicts the dominant contribution to the Marangoni stress and hence the direction of the flow along the interface for different $\bar{X}_a$. The variation of r about the mean value $\bar{r}$ is due to convection in the liquid layer, which should be suppressed for thin liquid films, since the Marangoni number scales with the square of the layer thickness d_l and the Rayleigh number scales as d_l^4 [11]. Hence, for sufficiently thin films, we should expect $r \approx \bar{r}$ and the interfacial flow velocity to be nearly uniform for all $\bar{X}_a$.

IV. CONCLUSIONS

By analyzing the comprehensive two-sided transport model for a volatile binary liquid driven by an externally applied temperature gradient [3] and its numerical solutions we demonstrated that, despite its complexity, the problem can be described analytically in certain useful limits. The analytical description best approximates the numerical results when the flow is relatively simple, with no spatially or temporally complicated convection pattern. In the presence of convection rolls, our analysis can predict with reasonable accuracy the mean flow and the mean gradients of various quantities, but not the spatial/temporal modulation describing the convective pattern.

In modeling two-phase flows, it is a common practice to either ignore transport in the gas phase or describe it through effective boundary conditions at the free surface. For volatile binary liquids, this approach fails in a rather spectacular manner. Our analysis shows that, for fluid layers with sufficiently high aspect ratio, the transport equations for mass, heat, and momentum can be solved sequentially, starting with the bulk concentration fields in the gas phase. These concentration fields determine the temperature and composition of the liquid layer at the interface and, consequently, the Marangoni (thermocapillary and solutocapillary) stresses. The Marangoni stresses, in turn, control the flow in the liquid layer, which eventually determines the bulk temperature and concentration field in the liquid and the flow in the gas layer, yielding a complete solution of the problem. This result generalizes a similar conclusion for two-phase flows of volatile simple fluids [5].

We derived explicit analytical expressions for the mean solutocapillary and thermocapillary stresses correctly which correctly predict when the direction of the interfacial flow reverses. In particular, solutocapillary stresses were found to vanish when the gas is predominantly air ($\bar{X}_a \to 1$), such as under ambient conditions, since phase change is greatly suppressed. In this limit thermocapillary stresses drive the interfacial flow in the direction opposite the temperature gradient. In the opposite limit, when the air is removed almost completely ($\bar{X}_a \to 0$), phase change is enhanced and solutocapillary stresses dominate, driving the flow in the direction of the temperature gradient. Interestingly, the thermocapillary stresses do not vanish in this limit for volatile binary liquids, unlike volatile simple liquids for which thermocapillary stresses completely disappear [5, 9]. For $\bar{X}_a \lesssim 0.3$, the ratio $\bar{r}$ of mean solutocapillary and thermocapillary stresses monotonically increases with decreasing $\bar{X}_a$ and approaches a constant that is greater than unity for water-methanol mixture.

Our results provide useful guidelines for choosing the

composition of binary coolants and the optimal operating conditions for thermal management applications. In particular, the concentration of air in a sealed cavity needs to be below 10% or so for the solutocapillarity to balance the adverse effect of thermocapillary stresses. Solutocapillary effect plays a beneficial role in general, helping drive the liquid coolant towards the hot spots. Due to the monotonic dependence of r on $\bar{X}_a$, it is beneficial to reduce the air concentration as much as possible. The optimal composition of the binary coolant, on the other hand, corresponds to a small, but finite value of the concentration of the more volatile component, e.g., $\bar{Y}_m \approx 0.05$ for a water-methanol mixture.

ACKNOWLEDGMENTS

This work was supported by the National Science Foundation under Grant No. CMMI-1511470.

REFERENCES

[1] N. di Francescantonio, R. Savino, A. Y., New Alcohol Solutions for Heat Pipes: Marangoni Effect and Heat Transfer Enhancement, Int. J. Heat Mass Transfer 51 (2008) 6199–6207.

[2] Y. Li, M. Yoda, An experimental study of buoyancy-Marangoni convection in confined and volatile binary fluids, Int. J. Heat Mass Trans. 102 (2016) 369–380.

[3] T. Qin, R. O. Grigoriev, A numerical study of buoyancy-Marangoni convection of volatile binary fluids in confined geometries, Int. J Heat Mass Transf. Under Review.

[4] R. Taylor, R. Krishna, Multicomponent mass transfer, vol. 2, John Wiley & Sons, 1993.

[5] T. Qin, R. O. Grigoriev, The effect of noncondensables on buoyancy-thermocapillary convection of volatile fluids in confined geometries, Int. J Heat Mass Transf. 90 (2015) 678–688.

[6] R. O. Grigoriev, T. Qin, The effect of phase change on stability of convective flow in a layer of volatile liquid driven by a horizontal temperature gradient, J. Fluid Mech. 838 (2018) 248–283.

[7] D. Kroger, W. Rohsenow, Condensation Heat Transfer in the Presence of a Noncondensable Gas, Int. J. Heat Mass Trans. 11 (1968) 15.

[8] P. F. Peterson, V. E. Schrock, T. Kageyama, Diffusion Layer Theory for Turbulent Vapor Condensation with Noncondensable Gases, Journal of Heat Transfer-Transactions of the Asme 115 (1993) 998–1003.

[9] T. Qin, Ž. Tuković, R. O. Grigoriev, Buoyancy-thermocapillary Convection of Volatile Fluids under their vapors, Int. J Heat Mass Transf. 80 (2015) 38–49.

[10] G. Vazquez, E. Alvarez, J. M. Navaza, Surface tension of alcohol water+ water from 20 to 50. degree. C, Journal of chemical and engineering data 40 (1995) 611–614.

[11] T. Qin, Ž. Tuković, R. O. Grigoriev, Buoyancy-thermocapillary convection of volatile fluids under atmospheric conditions, Int. J Heat Mass Transf. 75 (2014) 284–301.